



Sveriges lantbruksuniversitet
Swedish University of Agricultural Sciences

Faculty of Natural Resources and Agricultural Sciences
Department of Molecular Sciences

Characterization of core-shell oxide nanoparticles

Eline Goossens

Department of Molecular Sciences
Independent Project in Chemistry • Bachelor thesis • 15 hec • First cycle, G2E
Molecular Sciences, 2018:8
Uppsala, 2018

Characterization of core-shell oxide nanoparticles

Eline Goossens

Supervisor: Gulaim Seisenbaeva, Dept. of Molecular Sciences, SLU

Assistant supervisor: Ievgen Pylypchuk, Dept. of Molecular Sciences, SLU

Examiner: Vadim Kessler, Dept. of Molecular Sciences, SLU

Credits: 15 hec

Level: G2E

Course title: Independent Project in Chemistry - Bachelor thesis

Course code: EX0668

Program/education: Chemistry

Place of publication: Uppsala

Year of publication: 2018

Title of series: Molecular Science

Part number: 2018:8

Online publication: <http://stud.epsilon.slu.se>

Keywords: magnetic core-shell nanoparticles, characterization, iron oxide, silica

Sveriges lantbruksuniversitet
Swedish University of Agricultural Sciences

Faculty of Natural Resources and Agricultural Sciences
Department of Molecular Sciences

Abstract

The growing amount of applications of nanoparticles (NP) have led to concern for their possible harmful effect on human health and the leakage in the environment. Characterization and quantification of the content of NPs are of prime importance, especially methods to relate size, composition and morphology of the particles with the possibility of their detection and quantification.

Magnetic iron oxide core-shell nanoparticles, coated with a protective silica layer have been proven to be successful as adsorbents for water purification and hydrometallurgy of rare earth elements. Their growing applications in catalysis, medicine and protection of the environment make them highly interesting for further characterization.

The goal of this thesis project was to analyze and characterize these NPs for future applications and quantification with single particle ICP-MS (spICP-MS). Instrument difficulties made quantification with spICP-MS impossible, but the particles have been characterized in the solid state using environmental scanning microscopy with energy dispersion X-ray spectroscopy analysis (ESEM-EDS), atomic force microscopy (AFM), powder X-ray diffraction (PXRD) and Fourier transform infrared spectroscopy (FTIR). The nanoparticles in solution are also investigated with nanoparticle tracking analysis (NTA), dynamic light scattering (DLS), inductively coupled plasma mass spectroscopy (ICP-MS) and again with ESEM-EDS and AFM. The mean size results of these different methods were compared.

It was concluded that the iron oxide core-shell NPs were successfully encapsulated by a silica layer. The core consists mostly of magnetite (Fe_3O_4), but some oxidation to maghemite ($\gamma\text{-Fe}_2\text{O}_3$) has taken place. The particles are very polydisperse and the dispersion aggregates quickly, so no 'right' size can be determined.

Further research needs to be done for development of applications. External investigation for separation based on magnetic properties to determine the fraction Fe_3O_4 that has been oxidized to $\gamma\text{-Fe}_2\text{O}_3$ and method development with single particle ICP-MS is required.

Keywords: magnetic core-shell nanoparticles, characterization, iron oxide, silica

Nederlandstalige samenvatting

Het steeds groeiende aantal van toepassingen met nanopartikels (NP) heeft geleid tot bezorgdheid voor hun mogelijk schadelijk effect op de menselijke gezondheid en lekkage in het milieu. Karakterisatie en kwantificatie van de inhoud van NPs zijn van voornaam belang, hoofdzakelijk methodes waarmee grootte, compositie en morfologie van de partikels gelinkt worden aan hun mogelijkheid voor detectie en kwantificatie.

Magnetische ijzeroxide kern-schil nanopartikels, bedekt met een beschermende silica laag zijn succesvol toegepast als absorbentia voor waterzuivering en hydrometallurgie van zeldzame aarden. Hun groeiende applicaties in katalyse, geneeskunde en bescherming van het milieu maken hen zeer interessant voor verdere karakterisering.

Het doel van dit thesis project was om deze NPs te analyseren en te karakteriseren voor verdere applicaties en om ze te kwantificeren met single particle ICP-MS (spICP-MS). Instrument moeilijkheden maakten kwantificering via spICP-MS onmogelijk, maar de partikels zijn gekarakteriseerd in de vaste vorm met environmental scanning microscopie met energie dispersie X-straal spectroscopie analyse (ESEM-EDS), atoomkrachtmicroscopie (AFM), poeder X-straal diffractie (PXRD) en Fouriertransformatie infraroodspectroscopie (FTIR). De nanopartikels in oplossing zijn ook onderzocht met nanoparticle tracking analyse (NTA) en dynamische lichtstrooiing (DLS), inductief gekoppeld plasma massaspectrometrie (ICP-MS) en opnieuw met ESEM-EDS en AFM. De gemiddelde groottes verkregen met deze verschillende methoden werden onderling vergeleken.

Er werd geconcludeerd dat de ijzeroxide kern-schil NPs met succes zijn omvat door een silica laag. De kern bestaat voornamelijk uit magnetiet (Fe_3O_4), maar gedeeltelijke oxidatie naar maghemiet ($\gamma\text{-Fe}_2\text{O}_3$) heeft plaatsgevonden. De partikels zijn zeer polydispers en de dispersie aggregeert snel, waardoor geen 'juiste' grootte kan bepaald worden.

Verder onderzoek moet gebeuren voor de ontwikkeling van applicaties. Extern onderzoek voor separatie gebaseerd op magnetische eigenschappen om de fractie Fe_3O_4 die geoxideerd is naar $\gamma\text{-Fe}_2\text{O}_3$ te bepalen en ontwikkeling van een methode voor single particle ICP-MS is vereist.

Kernwoorden: magnetische kern-schil nanopartikels, karakterisering, ijzeroxide, silica

Table of contents

List of tables	6
List of figures	7
Abbreviations	9
1 Introduction	11
1.1 Iron oxide nanoparticles	12
1.2 Silica nanoparticles	12
2 Method	14
2.1 Environmental Scanning Electron Microscopy with Energy Dispersion X-Ray Spectroscopy (ESEM-EDS)	14
2.2 Atomic Force Microscopy (AFM)	16
2.3 Powder X-Ray Diffraction (PXRD)	18
2.4 Fourier-Transform Infrared Spectroscopy (FTIR)	19
2.5 Dynamic Light Scattering (DLS)	20
2.6 Nanoparticle Tracking Analysis (NTA)	21
2.7 Inductively Coupled Plasma Mass Spectrometry (ICP-MS)	22
3 Experimental	24
4 Results and discussion	25
4.1 Environmental Scanning Electron Microscopy with Energy Dispersive X-Ray Spectroscopy (ESEM-EDS)	25
4.2 Atomic Force Microscopy (AFM)	29
4.3 Powder X-Ray Diffraction (PXRD)	32
4.4 Fourier-Transform Infrared Spectroscopy (FTIR)	33
4.5 Dynamic Light Scattering (DLS)	34
4.6 Nanoparticle Tracking Analysis (NTA)	36
4.7 Inductively Coupled Plasma Mass Spectrometry (ICP-MS)	38
5 Conclusion	39
References	41
Acknowledgements	43

List of tables

Table 1. Isobaric interferences for Fe isotopes with quadrupole ICP-MS	22
Table 2. The molar ratios of the non-dispersed FeO _x &SiO ₂ NPs measured with ESEM-EDS	27
Table 3. Identification of the peaks in the infrared spectrum	33
Table 4. The tested combinations for the optimal dispersion of the FeO _x &SiO ₂ NPs.	34
Table 5. Measured size and concentration of the newer and older sample of FeO _x &SiO ₂ NPs with NTA.	36
Table 6. Measured total concentration of FeO _x &SiO ₂ NPs with ICP-MS.	38
Table 7. Comparison of the measured mean sizes obtained with ESEM-EDS, AFM, DLS and NTA of the FeO _x &SiO ₂ NPs.	39

List of figures

<i>Figure 1.</i> Schematic representation of the scanning electron microscope (SEM).	14
<i>Figure 2.</i> Schematic representation of the atomic force microscope (AFM).	16
<i>Figure 3.</i> The non-dispersed FeO _x &SiO ₂ NPs as measured by ESEM-EDS. Magnetization from left to right, top to bottom: 500x, 2500x, 5000x and 10 000x (scale bar is 200, 30, 20 and 10 μm respectively).	25
<i>Figure 4.</i> The non-dispersed FeO _x .SiO ₂ NPs as measured by ESEM-EDS, with measured sizes. Magnetization 10 000x and scale bar 10 μm.	26
<i>Figure 5.</i> EDS graph of the non-dispersed FeO _x &SiO ₂ NPs, taken with 5000x magnetization	26
<i>Figure 6.</i> The dispersed FeO _x &SiO ₂ NPs as measured by ESEM-EDS. Magnetization from left to right: 6000x and 10 000x (scale bar is 10 μm for both).	27
<i>Figure 7.</i> The dispersed FeO _x &SiO ₂ NPs as measured by ESEM-EDS, with measured sizes. Magnetization 10 000x and scale bar 10 μm.	28
<i>Figure 8.</i> HR-TEM images of FeO _x &SiO ₂ NPs (scale bar is 100, 20 and 5 nm for A), B) and C) respectively). D) is the EF-TEM image. Reproduced with permission from the publisher from ref. (Legaria et al., 2015).	29
<i>Figure 9.</i> The non-dispersed FeO _x .SiO ₂ NPs as measured by AFM.	30
<i>Figure 10.</i> The dispersed FeO _x &SiO ₂ NPs as measured by AFM.	31
<i>Figure 11.</i> The FeO _x &SiO ₂ NP spectrum as measured by PXRD. The blue line is the sample, the red peaks correspond to Fe ₃ O ₄ and the green peaks correspond to SiO ₂ .	32
<i>Figure 12.</i> The FeO _x &SiO ₂ spectrum as measured by FTIR.	33
<i>Figure 13.</i> Z-average diameter measured with DLS after 0 and 15 hours of preparation	35
<i>Figure 14.</i> The particle size distribution of the FeO _x &SiO ₂ NPs as measured with DLS.	35
<i>Figure 16.</i> The particle size / concentration plot and particle size / relative intensity 3D plot of the older sample of FeO _x &SiO ₂ NPs as measured with NTA (mean size 299 nm and total concentration 0.39 * 10 ⁸ particles mL ⁻¹).	37

Figure 15. The particle size / concentration plot and particle size / relative intensity 3D plot of the newer sample of FeO_x&SiO₂ NPs as measured with NTA (mean size 199 nm and total concentration 0.14 * 10⁸ particles mL⁻¹). 37

Abbreviations

AFM	Atomic Force Microscopy
AMU	Unified Atomic Mass Unit
BSE	Back Scattered Electron
CCD	Charge Coupled Device
CCT	Collision Cell Technology
DLS	Dynamic Light Scattering
EDL	Electronic Double Layer
EF-TEM	Energy Filtered Transmission Electron Microscopy
ESEM-EDS	Environmental Scanning Electron Microscope - Energy Dispersion X-Ray Spectroscopy
FTIR	Fourier Transform Infrared Spectroscopy
HR-TEM	High Resolution Transmission Electron Microscopy
ICP-MS	Inductively Coupled Plasma Mass Spectrometry
KED	Kinetic Energy Discrimination
MC	Microcystin
MRI	Magnetic Resonance Imaging
NP	Nanoparticle
NTA	Nanoparticle Tracking Analysis
PSD	Particle Size Distribution
PXRD	Powder X-Ray Diffraction
REE	Rare Earth Element
SE	Secondary Electron
spICP-MS	Single Particle ICP-MS
SPM	Scanning Probe Microscopy
TEOS	Tetraethyl Orthosilicate

1 Introduction

Magnetic iron oxide core-shell nanoparticles (NP), coated with a protective silica layer, have been successfully implemented in various wide applications such as bio separation, enzyme immobilization, diagnostic analysis and so on (Deng *et al.*, 2008). The specific nanoparticles of this kind that were used in this thesis were synthesized by the molecular sciences department to be used as adsorbents for water purification and hydrometallurgy of rare earth elements (REE) by Seda Demirel Topel (2014).

The goal was to characterize and quantify the content of these NPs for future applications and compare their possibility of detection and quantification with different analytical methods. The particles were designed to have a mean size of 80 nm via the Stöber method, which normally gives a narrow size distribution.

An example of a possible application of $\text{FeO}_x\&\text{SiO}_2$ NPs comes from a 2011 study by Wang *et al.* (2011), which demonstrated the potential of $\text{Fe}_3\text{O}_4\&\text{SiO}_2$ NPs grafted with folic acid - conjugated polyglycerol for targeting ovarian cancer cells in magnetic resonance imaging (MRI). Another example is the catalytic ability of $\text{Fe}_3\text{O}_4\&\text{SiO}_2\&\text{Schiff}$ base complex, which showed to be an efficient catalyst for conversion of aldehydes to 1,1-diacetates that can easily be recovered and reused at least five times without deterioration in catalytic activity (Esmailpour *et al.*, 2012).

Water purification is, given the growing industrialization and use of chemicals for various applications, a continuous subject of interest for research. One example of the applicability of the $\text{Fe}_3\text{O}_4\&\text{SiO}_2$ NPs in this field is an article by Deng *et al.* (2008). In this research, the NPs were found to be suitable as a reusable absorbent for fast and highly efficient removal of microcystins (MC), a class of toxins produced in cyanobacterial blooms, in many eutrophic waters.

REEs are a group of 17 elements with unique magnetic and conductive properties that are used in many different applications, the most common being high-tech products. They've been declared as strategic and/or raw materials, which contributes to the increasing interest for new methods in extraction and separation of REEs (Legaria, 2018). It has been demonstrated that the Fe_3O_4 & SiO_2 NPs can be used as adsorbents for several REE ions (Legaria, 2018) and can easily be desorbed. Besides that, they can also be used as a luminescent probe to detect the ions solution (Topel et al., 2014).

1.1 Iron oxide nanoparticles

Iron oxides (and oxide-hydroxides) are common in the environment, where they play a role in multiple geological and biological processes. The most common iron oxide phases are magnetite (Fe_3O_4), maghemite ($\gamma\text{-Fe}_2\text{O}_3$) and hematite ($\alpha\text{-Fe}_2\text{O}_3$) (Cornell and Schwertmann, 2003).

Maghemite can be considered as an intermediate form of magnetite and hematite. It is isostructural with magnetite, but with cation deficient sites. Both forms possess the inverse spinel structure (Haneda and Morrish, 1977). The main thing that differentiates these two iron oxides is that magnetite consists of ferrous (Fe^{2+}) and ferric (Fe^{3+}) ions, while maghemite only has ferric ions, they can thus be transformed into one another via redox mechanisms.

While magnetite has the most dominant magnetic properties, it is easily oxidized to maghemite due to its instability as a NP. This results in a decrease of magnetization, but in general these maghemite NPs obtain enough magnetic aspects for their intended purpose (Legaria, 2018).

Magnetite NPs have been used in numerous applications such as tissue-specific releasing of therapeutic agents, labeling and sorting of cells and separation of biochemical products (Hui et al., 2011). More recently the NPs have also gained interest in biomedicine and bio sensing (Sun and Zeng, 2002).

1.2 Silica nanoparticles

Silica (SiO_2), the most abundant compound found in earth's crust, is widely used in a variety of functions. This ranges from high-tech applications to being used as an additive in food production (Encyclopedia, 2018b).

While crystalline silica is proven to be toxic upon inhalation, the effect on human health of SiO_2 NPs is still a topic of discussion (Murugadoss et al., 2017). The NPs

possess much greater surface area than the bulk material, resulting in more adsorption potential.

The many recently published articles regarding this topic display the huge interest in silica NPs for biomedical applications, drug delivery, catalytic purposes, etc. The NPs exhibit several promising properties, such as excellent biocompatibility, thermal stability and an easy and well-characterized synthetic route via the Stöber method, which is an alkaline hydrolysis of tetraethyl orthosilicate (TEOS), (Stober et al., 1968, Murugadoss et al., 2017). NPs synthesized via this Stöber method still contain some silanol (SiOH) groups on the surface, which makes it relatively simple to further functionalize them. Surface modifications such as amino, thiol and carboxyl groups allow the control of surface chemistry for site-specific targeting and selective adsorption, among other things (Legaria, 2018).

One major disadvantage is the challenges in removal of the silica NPs from the solution, which is done with expensive and time-consuming centrifugation. For this reason, the iron core-shell magnetic silica particles were synthesized. They combine all the beneficial properties of SiO₂ NPs with the easy removal of the magnetic NPs. Another reason is that iron oxide magnetic NPs are unstable in harsh conditions such as acidic media, which calls requires the use of a protective layer. Among all the advantages just described, silica is also highly stable in aqueous conditions and enhances the biocompatibility, hydrophilicity and dielectric properties (Legaria, 2018). A silica layer of approximately 25 nm in thickness has been proven to provide optimal balance between protecting the core, while still maintaining the desired magnetic properties (Pogorilyi et al., 2014). As previously mentioned, encapsulation of magnetite NPs leads to some oxidation to the less magnetic form maghemite.

2 Method

What follows is a brief explanation of different techniques used for the NP characterization. The particles were analyzed in solid state and in dispersion using microscopy techniques (ESEM-EDS and AFM) and just in the solid state with X-Ray Diffraction (PXRD) and Infrared spectroscopy (FTIR). The suspension of NPs has also been investigated using DLS, NTA and ICP-MS.

2.1 Environmental Scanning Electron Microscopy with Energy Dispersion X-Ray Spectroscopy (ESEM-EDS)

Scanning Electron Microscopy (SEM) is a microscopy technique that can construct images of a sample. Figure 1 shows different parts that make up the electron microscope. An electron gun produces a primary electron beam, which is focused by an electromagnetic lens system onto the sample. The beam scans the surface, causing the electrons to interact with the atoms in the sample (Course-material, 2015). Scanning occurs in a raster scan pattern. By altering the acceleration voltage, the interaction volume can be varied.

This interaction produces two types of scattered electrons: secondary electrons (SE) and back scattered electrons (BSE). SEs and BSEs both have an individual detector and are used together for imaging in SEM. Secondary electrons are generated from

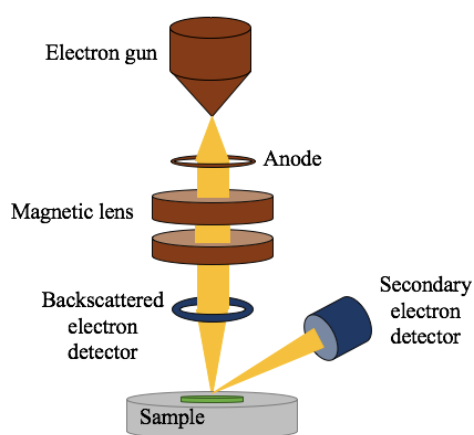


Figure 1. Schematic representation of the scanning electron microscope (SEM).

inelastic scattering of the beam, which occurs when the interacting primary electrons have low energy (< 50 eV). They are typically used for topography and morphology. Since they have low energy, only SE's formed close to the surface and short distance of the beam can escape the specimen and contribute to the signal (Holbrook et al., 2015).

The back scattered electrons are generated from elastic scattering. They are primary electrons with higher energy (≥ 50 eV) that keep their energy and velocity during change of direction (Course-material, 2015, Holbrook et al., 2015). BSEs also present information about the sample composition. Atoms with a higher mass backscatter more strongly, so the intensity in a BSE image is proportional to the atomic number of the atoms present in the sample (Holbrook et al., 2015).

Conventional SEM observes samples in high vacuum, since a gas atmosphere spreads rapidly and would attenuate electron beams. The sample should also have a conductive surface to prevent accumulation of charge, as the electron beam produces an electric current. As a result, samples that create some vapor need to be dried or cryogenically frozen and examining an insulating surface is out of the question.

However, Environmental SEM (ESEM) can operate in low vacuum or 'wet' conditions in variable pressure by allowing for a gaseous environment in the specimen chamber. The presence of an ionized gas also clears the produced current on the sample surface, eliminating the need for pre-treatment of samples to make the surface conductive.

The use of gas was made possible by using a specialized secondary-electron detector that was able to operate in the presence of water vapor via differential pumping systems. The secondary electrons are accelerated towards the electric field of the detector. By colliding with the gas molecules, more free electrons are generated that result in a signal. The positive gas ions furthermore neutralize the excess of charge on the sample.

By coupling ESEM to Energy-Dispersive X-Ray Spectroscopy (EDS), different elements in the sample can be identified. Each element has a unique atomic structure. When inner-shell electrons are ejected from the sample due to the inelastic scattering, an outer-shell electron fills the vacant spot. Energy is released during this process in the form of element specific X-rays, since the X-ray energy equals the difference in the energy levels between the outer-shell and ejected inner-shell electrons (Holbrook et al., 2015). The EDS detector generates the energy and intensity distribution of samples. A sample can be analyzed qualitative, by looking at the position of the peaks, and quantitative, by relating the relative height of the peak to the con-

centration. (Encyclopedia, 2018a) Where modern EDS detectors can identify all elements, earlier types can only detect elements with a molar mass greater than that of Na, removing the possibility of detection for elements such as C, N and O.

2.2 Atomic Force Microscopy (AFM)

Atomic Force Microscopy (AFM) is a type of Scanning Probe Microscopy (SPM), which means it is based on measurements of the interactions between the sample surface and the probe on a small distance. It has developed the most rapidly out of all types of SPM, since it can be applied to non-conductive samples in a wide range of media (Wilkinson and Lead, 2007). As illustrated in figure 2, it consists of a cantilever with a probe at the end. The tip of the probe can move in a horizontal or vertical direction in a grid pattern.

When the tip, which has a radius of curvature of only a few nanometers, is brought close to the surface, forces (van der Waals forces, electrostatic forces, magnetic forces etc., depending on the situation) between the tip and the sample lead to

a deflection of the cantilever according to Hooke's law:

$$F = kX$$

with k the cantilever spring constant and X the deflection of the extremity of the cantilever (Wilkinson and Lead, 2007).

The cantilever's deflection is visualized by a laser light that's reflected from the back of the cantilever onto a highly sensitive photodiode. The reflected light is bent under an angle dependent on the height. By adjusting the sample height, a constant force is used on the tip. The recorded adjustments are translated into a 3D map of the surface (Holbrook et al., 2015).

There exist several imaging modes for AFM, the most important ones being contact, tapping and non-contact. Contact mode is the most conventional and brings the tip in close contact with the surface. When a voltage is applied, the cantilever is attracted to the sample, but when reaching sufficiently small distances the probe is

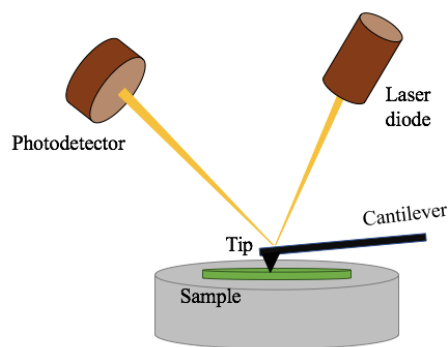


Figure 2. Schematic representation of the atomic force microscope (AFM).

deflected by sample-probe interaction forces. This gives a constant vertical movement towards and away from the sample. In contact mode, the tip of the probe is put into the repulsive zone. This method has some limitations, the main one being that there are significant lateral forces by the dragging motion of the tip.

The tapping mode (also known as intermittent mode) and non-contact mode overcome this restraint. In tapping mode, the cantilever oscillates at its resonance frequency. As the probe enters the repulsive zone, this oscillation is changed. The feedback signal when trying to maintain a constant amplitude is used to generate an image. The non-contact mode operates similarly, but the cantilever now oscillates in the attractive zone. The tapping mode is usually preferred over the non-contact mode, due to the larger instability of the attractive signal (Wilkinson and Lead, 2007).

The techniques as described above are all for topographical imaging. Changes in the phase angle of the resonance frequency can also produce a second image by a technique called phase imaging.

The resolution of the measured lateral distance is limited by the curvature of the tip, so for NPs that are of sizes similar to or smaller than the curvature, height measurements are deemed to be more accurate. These achieve Angstrom-level resolution (Holbrook et al., 2015). Measurements are only possible for NPs that are well-dispersed and adequately attached to the substrate. (Wilkinson and Lead, 2007)

Besides imaging, AFM can also be used for force measurement and manipulation.

2.3 Powder X-Ray Diffraction (PXRD)

Powder X-Ray Diffraction is used for structural characterization of a sample. Crystalline materials consist of a periodic matrix, which forms repetitive layers (Course-material, 2015). When an X-ray source impacts on the sample surface, the X-rays are diffracted into several specific directions. This produces bright spots at particular angles due to constructive interference. The atoms in the sample thus act as a diffraction grating and by measuring the angle where these intensity maxima occur, the spacing can be calculated by Bragg's equation: (Holbrook et al., 2015)

$$2d \sin \theta = n\lambda$$

where d = the interlayer distance, θ = the inclination angle, n = the positive integer indicating the diffraction magnitude and λ = the wavelength.

Powder samples can be seen as a collection of small crystals, each with different orientation. When an X-ray hits crystalline powder, many single spots will be produced on the detector. These spots merge together into rings, an effect that is enhanced by also rotating the sample in the beam. After integrating the produced photograph, an X-ray powder diffraction pattern is obtained (Course-material, 2015). The collected pattern is a result of all particles in the examined volume, making characterization of individual particles usually impossible (Holbrook et al., 2015). This pattern is matched to a structure database with known crystal structures to determine the composition of the sample. Attention has to be paid to the fact that isostructural minerals can have X-ray patterns that are very close (Course-material, 2015).

2.4 Fourier-Transform Infrared Spectroscopy (FTIR)

Fourier-Transform Infrared Spectroscopy (FTIR) provides an easy way to identify certain functional groups in a molecule. An infrared spectrum of absorption or emission is obtained, which is characteristic of the structure of the sample. Almost all compounds absorb IR radiation, which lies between visible light and microwaves in the electromagnetic spectrum. Only compounds that don't have a dipole moment that changes with time, don't absorb IR radiation (Pavia et al., 2008).

IR is divided into three sections: near IR (13 000 - 4000 cm^{-1}), mid IR (4000 - 400 cm^{-1}) and far IR (400 - 10 cm^{-1}). The wavenumber ν has the reciprocal centimeter as unit, it is proportional to the frequency of the radiation. When IR radiation is absorbed by a molecule, which is always a quantized process, it causes this molecule to vibrate. The types of molecular vibrations can be classified into two types: stretching, where the bond length changes and bending, where the bond angle changes (also known as deformation). There are 6 types of fundamental vibrations: symmetrical stretching ν_s , asymmetrical stretching ν_{as} , in-plane bending δ (scissoring), in-plane bending ρ (rocking), out-of-plane bending ω (wagging) and out-of-plane bending τ (twisting).

The frequencies of IR radiation that match the natural vibration frequencies of the molecule are absorbed and this absorption increases the amplitude (Pavia et al., 2008). These frequencies are thus distinctive for their structure; each functional group gives rise to a characteristic band. Besides position (frequency) of the peaks, they can also be distinguished by intensity. This information is usually summarized in infrared correlation tables.

An FTIR spectrometer can measure high-spectral-resolution data over a wide spectral range. As the name indicates, the mathematical operation Fourier transform is used to convert the raw data into a spectrum. The produced pattern by the spectrometer is the complex interferogram, a plot of intensity vs time. The Fourier transform separates the individual frequencies from the interferogram, resulting in the desired intensity vs frequency plot. A FTIR spectrum obtains spectra faster and with greater sensitivity than a conventional dispersion instrument (Pavia et al., 2008).

2.5 Dynamic Light Scattering (DLS)

Dynamic Light Scattering (DLS, also called Photon Correlation Spectroscopy or Quasi-Elastic Light Scattering) is a non-destructive technique used to determine the size distribution of small particles in suspension (Holbrook et al., 2015). A monochromatic light source is directed at the suspension, where it is scattered. Suspended particles follow the Brownian motion, which describes their random movement resulting from the collisions with molecules in the fluid (Brittanica, 2017). Due to this Brownian motion, the scattering intensity fluctuates with time, since the distances between the particles constantly change. By computing an intensity correlation coefficient of the Doppler shifts of scattered light over time, a z-averaged diffusion coefficient D_z is obtained. This diffusion coefficient is used to determine the hydrodynamic radius of the particle via the Stokes-Einstein equation, assuming the NP is spherical: (Domingos et al., 2009, Holbrook et al., 2015)

$$D = \frac{k_b T}{6\pi\eta r}$$

where k_b = the Boltzmann constant, T = the absolute temperature, η = the viscosity and r = the radius.

The observed scattering intensity is a function of several parameters: the scattering angle, particle size and shape, instrument optics and measurement duration. This makes it difficult to obtain a true particle size distribution (PSD) via DLS (Holbrook et al., 2015).

It has been found that DLS may overestimate particle sizes, likely due to light scattering principles. Relatively high concentrations are required to scatter enough light (Domingos et al., 2009).

Dispersion stability

When trying different method to find the optimal dispersion, increasing the pH also increases the stabilization. A charge is introduced on the particle surface, resulting in a surface potential. The surface charge, consisting of adsorbed ions, attracts a second layer of counter-ions, extending into the solution and repulsing other particles. These two layers together form the electrical double layer (EDL), acting as an energy barrier formed by the repulsive force and preventing two particles from approaching one another. The degree of EDL charge can be estimated with the electrokinetic zeta potential, which is defined as the potential at the slipping plane between the particle and the associated double layer.

The magnitude of zeta potential indicated the degree of repulsion between the particles, making it an indicator for dispersion stability. As the pH of the solution increases, the zeta potential becomes more negative. A zeta potential of more than 40 mV results in good to excellent stability. (Larsson et al., 2012).

2.6 Nanoparticle Tracking Analysis (NTA)

Nanoparticle Tracking Analysis (NTA) is used to visualize and analyze suspended particles and produce a size distribution profile. It has many similarities with DLS: both measure the diffusion constant D_z of the Brownian motion and use this to calculate the particle size via the Stokes-Einstein equation. However, where DLS analyses the scattering intensity fluctuations, NTA tracks individual trajectories of particles and uses the mean squared travelled distances for the diffusion coefficient. This eliminates the limitation of using a z-average distribution. A charge-coupled device (CCD) camera is used for the visualization and recording of the particle movement (Domingos et al., 2009).

NTA has, just like DLS, a bias towards larger particles. Nonetheless the effect of larger particles masking smaller particles is reduced compared to DLS. A relatively high concentration is again needed for analysis (Domingos et al., 2009).

2.7 Inductively Coupled Plasma Mass Spectrometry (ICP-MS)

For a more extensive review of ICP-MS and single particle ICP-MS (spICP-MS) the reader is referred to the other thesis (*Size detection limits of spICP-MS for analysis of nanoparticles in environmental media*).

Quadrupole ICP-MS is plagued by isobaric interferences, which can occur between any combination of atomic, molecular or doubly charged ions that have nearly equal mass to charge ratio (m/z). When measuring Fe with ICP-MS, which most common isotope has a mass of 55.93 amu (unified atomic mass unit) there is always spectral interference with $^{40}\text{Ar}^{16}\text{O}^+$, among other polyatomic ions, as can be seen in table 1. (May and Wiedmeyer, 1998).

Table 1. *Isobaric interferences for Fe isotopes with quadrupole ICP-MS*

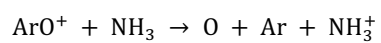
Isotope	Abundance (%)	Interference
^{54}Fe	5,82	$^{37}\text{Cl}^{16}\text{O}^1\text{H}^+$, $^{40}\text{Ar}^{14}\text{N}$, $^{38}\text{Ar}^{15}\text{N}^1\text{H}^+$, $^{36}\text{Ar}^{18}\text{O}^+$, $^{38}\text{Ar}^{16}\text{O}^+$, $^{36}\text{Ar}^{17}\text{O}^1\text{H}^+$, $^{36}\text{S}^{18}\text{O}^+$, $^{35}\text{Cl}^{18}\text{O}^1\text{H}^+$, $^{37}\text{Cl}^{17}\text{O}$
^{56}Fe	91,66	$^{40}\text{Ar}^{16}\text{O}^+$, $^{40}\text{Ca}^{16}\text{O}^+$, $^{40}\text{Ar}^{15}\text{N}^1\text{H}^+$, $^{38}\text{Ar}^{18}\text{O}^+$, $^{38}\text{Ar}^{17}\text{O}^1\text{H}^+$, $^{37}\text{Cl}^{18}\text{O}^1\text{H}^+$
^{57}Fe	2,19	$^{40}\text{Ar}^{16}\text{O}^1\text{H}^+$, $^{40}\text{Ca}^{16}\text{O}^1\text{H}^+$, $^{40}\text{Ar}^{17}\text{O}^+$, $^{38}\text{Ar}^{18}\text{O}^1\text{H}^+$, $^{38}\text{Ar}^{19}\text{F}^+$
^{58}Fe	0,33	$^{40}\text{Ar}^{18}\text{O}^+$, $^{40}\text{Ar}^{17}\text{O}^1\text{H}^+$

It has been proven that collision-reaction cell technology can be used for removing this interference (Tanner et al., 2002). It is a relatively new method for removing interfering species before they reach the mass analyzer. The cell is filled with a gas and the interferences may be removed by the following mechanisms:

- Collisions: The molecular ions will lose kinetic energy, or even dissociate upon colliding with an inert gas (most often He). Kinetic energy discrimination (KED) is placed after the collision cell and the probability of the ions that have undergone a collision to pass it is reduced. Analyte ions will also collide in some extent, however, the probability for so happening is lower than for the molecular ions because of the smaller size.
- Reactions: Interferents can also be removed with selective oxidation with gases such as O_2 or NH_3 . Based on ionization-energies it can be predicted which reaction gases could transfer an electron to the interferent before the analyte ion (Thomas, 2002, Montano et al., 2016).

When using collisions with He-gas the molecular ions lose kinetic energy and can be removed via kinetic energy discrimination (KED). However, the reaction gas

NH₃ has been found to be one of the most effective applications for the charge exchange between Ar and NH₃, removing the interference at $m/z = 56$.



Since Fe has an ionization potential of 7.902 eV, NH₃ an ionization potential of 10.200 eV and Ar one of 15.760 eV, this exothermic reaction takes almost completely place between argon and ammonia and not iron.

3 Experimental

- ESEM-EDS experiments were done on a Perkin Elmer TM-1000- μ -DEX scanning electron microscope.
- AFM measurements were done on a Bruker Fastscan in Scanasyst mode. A silicon tip on silicon nitride cantilever in mode Fastscan-B was used.
- PXRD experiments were carried out with a multi-purpose Bruker SMART Apex II-Instrument. The background subtraction and the pattern identification were made using Bruker EVA-12 program
- The FTIR spectrum was recorded as KBr pellets on a Perkin Elmer Spectrum 100 instrument.
- DLS experiments were carried out on the Malvern Panalytical Zetasizer Nano ZS instrument.
- NTA experiments were carried out on the Malvern Panalytical Nanosight NS300 instrument.
- All ICP-MS measurements were done on a Perkin Elmer quadrupole ICP-MS (NexION 350). For spICP-MS, the Nano Syngistix app was used.

4 Results and discussion

4.1 Environmental Scanning Electron Microscopy with Energy Dispersive X-Ray Spectroscopy (ESEM-EDS)

Figure 3 shows the nanoparticles as seen by ESEM-EDS when they are not dispersed.

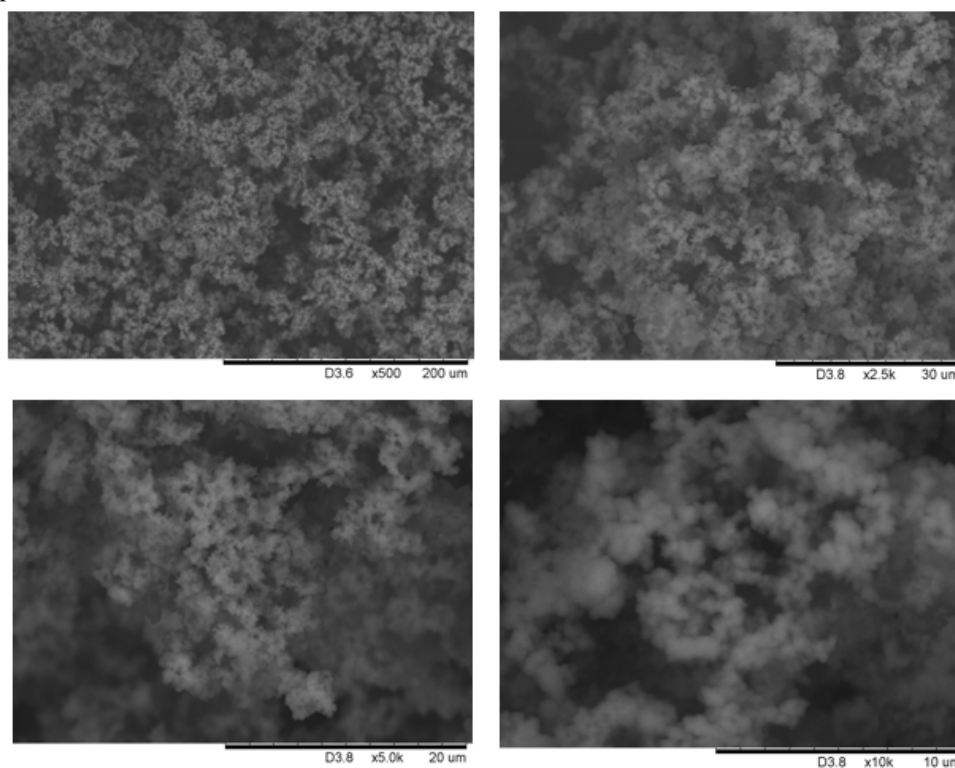


Figure 1. The non-dispersed FeO_x&SiO₂ NPs as measured by ESEM-EDS. Magnetization from left to right, top to bottom: 500x, 2500x, 5000x and 10 000x (scale bar is 200, 30, 20 and 10 μm respectively).

The particles are visibly aggregated because of their magnetic nature. When the NP size is measured, the results vary from 610 to 809 nm, with an average of 738 nm, as can be seen in figure 4. It is indicated where the aggregates were being measured.

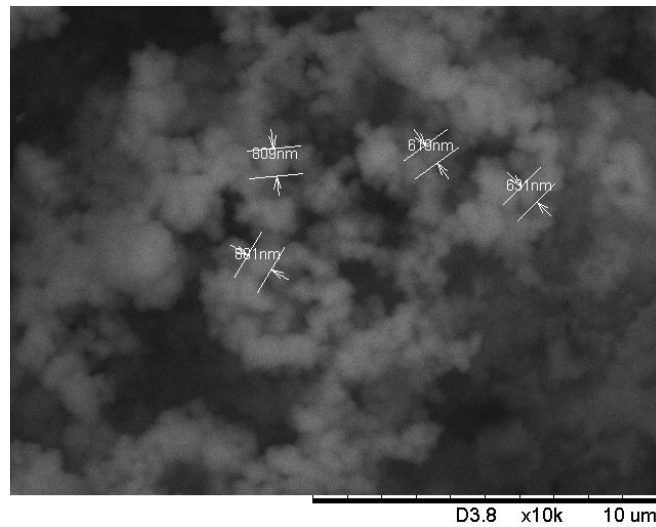


Figure 2. The non-dispersed FeO_xSiO_2 NPs as measured by ESEM-EDS, with measured sizes. Magnetization 10 000x and scale bar 10 μm .

As explained, ESEM can also provide information about the composition of a sample when it's coupled to EDS. An example of the results is shown below in figure 5 and table 1.

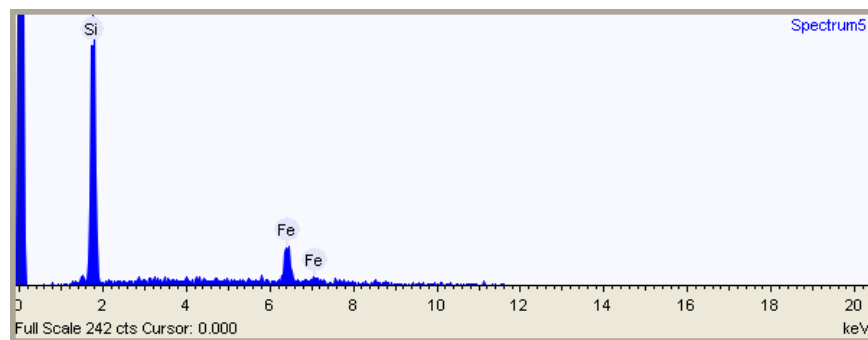


Figure 3. EDS graph of the non-dispersed FeO_xSiO_2 NPs, taken with 5000x magnetization

The nanoparticles consist of iron oxides and silica and consequently there's a significant amount of oxygen which can't be detected by this type of EDS. This results in the big peak at 0 keV. Silicon and iron are successfully detected, each peak corresponds with a different excitation-level. Sometimes a peak of aluminum can also be seen, which originates from the holder the sample was put on.

The resulted weight % is divided by the molar mass of silicon and iron (28.0855 amu and 55.854 amu respectively) to get the molar ratio. There are variations in the resulted ratios, depending on where in the sample the results were obtained. This is because the iron core isn't always completely covered by silica and the distribution of iron particles in one nanoparticle varies. Both factors are impossible to fully control during the synthesis. ESEM-EDS also isn't reliable enough for quantitative determination of the elements, since it is strongly influenced by several factors such as homogeneity and/or smoothness of the sample surface. Nevertheless, it is good for qualitative determination and proves that the sample mostly consists of Si and Fe, corresponding with silica and iron oxide.

To account for these irregularities, several measurements of the ratios were done on different places in the sample and the average was calculated. The results can be seen in the table below:

Table 2. The molar ratios of the non-dispersed FeO_x & SiO_2 NPs measured with ESEM-EDS

Magnitude	500x	2500x	5000x	5000x	5000x	Average
Si : Fe ratio	2.51 : 1	6.33 : 1	5.43 : 1	2.05 : 1	2.80 : 1	3.83 : 1

The nanoparticles were dispersed in 0.1 mM NaOH (reasoning behind this is described further on) and measured again, the results are shown in figure 6.

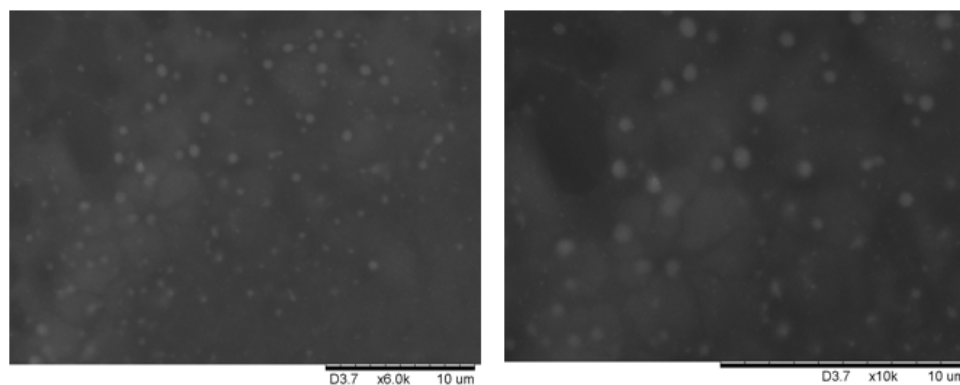


Figure 4. The dispersed FeO_x & SiO_2 NPs as measured by ESEM-EDS. Magnetization from left to right: 6000x and 10 000x (scale bar is 10 μ m for both).

The resolution of this specific ESEM instrument was insufficient to get sharp images of the smallest NPs, but the spherical shape of the particles can be seen. Some crystallization of NaOH can be also observed. The measured sizes are shown in figure 7. Only the aggregates and biggest particles could be seen, so the average size of 627 nm is likely a lot bigger than the actual average size. Some lower sizes of 208 nm and 442 nm are also achieved.

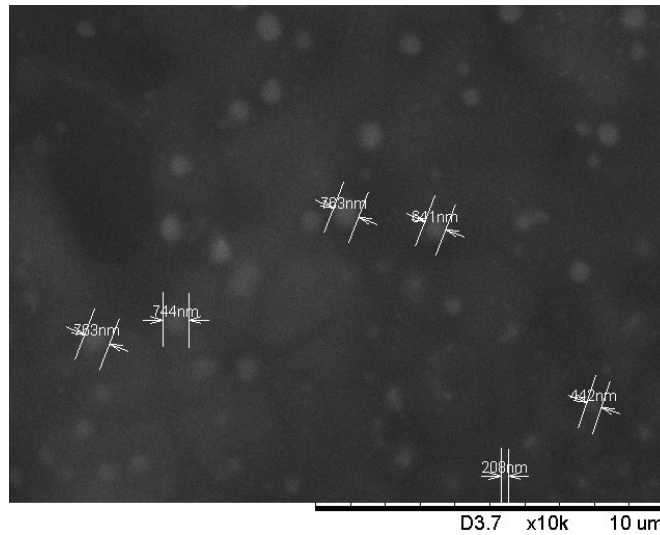


Figure 5. The dispersed $\text{FeO}_x/\text{SiO}_2$ NPs as measured by ESEM-EDS, with measured sizes. Magnetization 10 000x and scale bar 10 μm .

The concentration was too low to accurately measure the composition. No iron was measured, except for one example, which resulted in a Si : Fe : Na ratio of 17.91 : 1.14 : 1. Since one measurement doesn't hold any statistical relevance, the average molar ratio of the non-dispersed NPs is deemed to be the most accurate.

High resolution transmission electron microscopy (HR-TEM) results acquired by Legaria *et al.* (2015) of the NPs showed the particles have an average diameter of 100 nm (± 15 nm). Figure 8 shows the images, where can be seen that a uniform coating is achieved. Figure 8D shows the mapping of the iron in green and silicon in red elements. This confirms that the NPs have a core-shell structure.

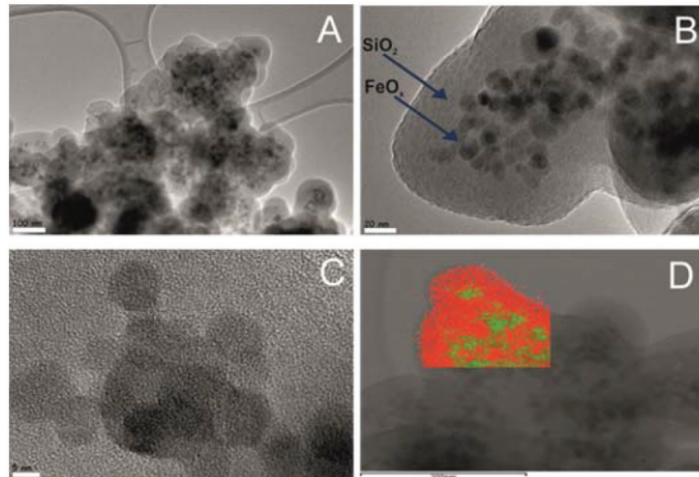


Figure 8. HR-TEM images of FeO_x&SiO₂ NPs (scale bar is 100, 20 and 5 nm for A), B) and C) respectively). D) is the EF-TEM image. Reproduced with permission from the publisher from ref. (Legaria et al., 2015).

4.2 Atomic Force Microscopy (AFM)

The AFM images obtained of the non-dispersed NPs are shown in figure 9, while figure 10 shows the images of the dispersed NPs.

The AFM results give a bias towards smaller particles.

There is a lot of size variation. In the images of the dispersed NPs, extremely small particles can be seen, which are in the range of ~ 1 nm. For the non-dispersed NPs, aggregation can clearly be seen. A non-aggregated NP was found in the non-dispersed sample, which gave a size result of ~ 90 nm. Other sizes vary between ~130 and 180 nm, but these are always the result of an aggregation. Separate particles can more easily be found in the dispersed sample, however the particles shifted when being measured, so aggregates needed to be analyzed for correct results. The dispersed particles seem to be ~ 30 nm or bigger.

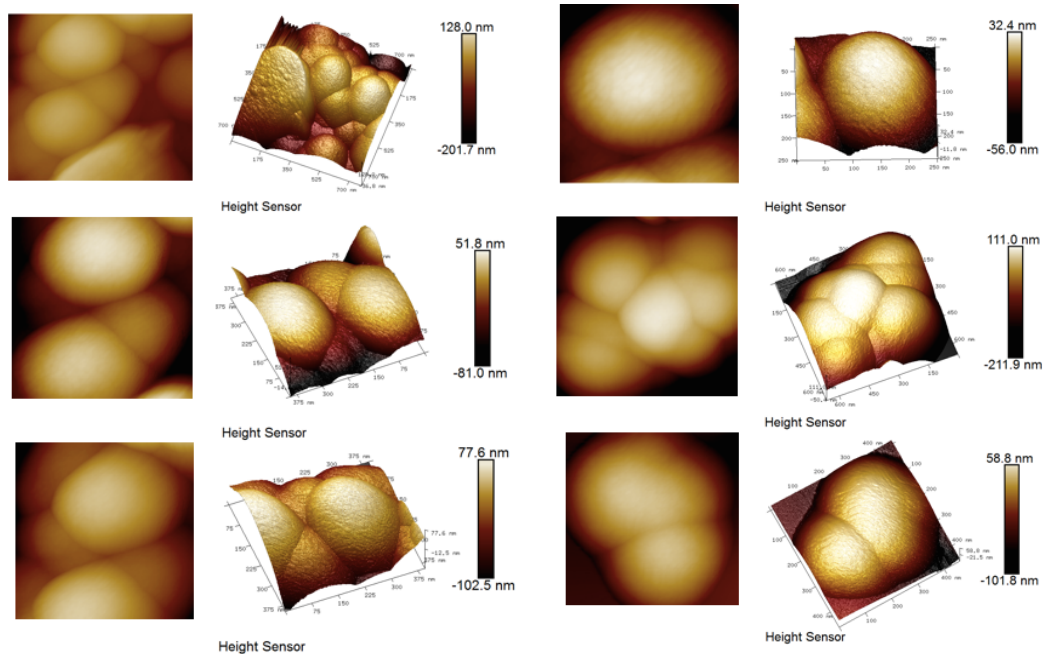


Figure 9. The non-dispersed $\text{FeO}_x.\text{SiO}_2$ NPs as measured by AFM.

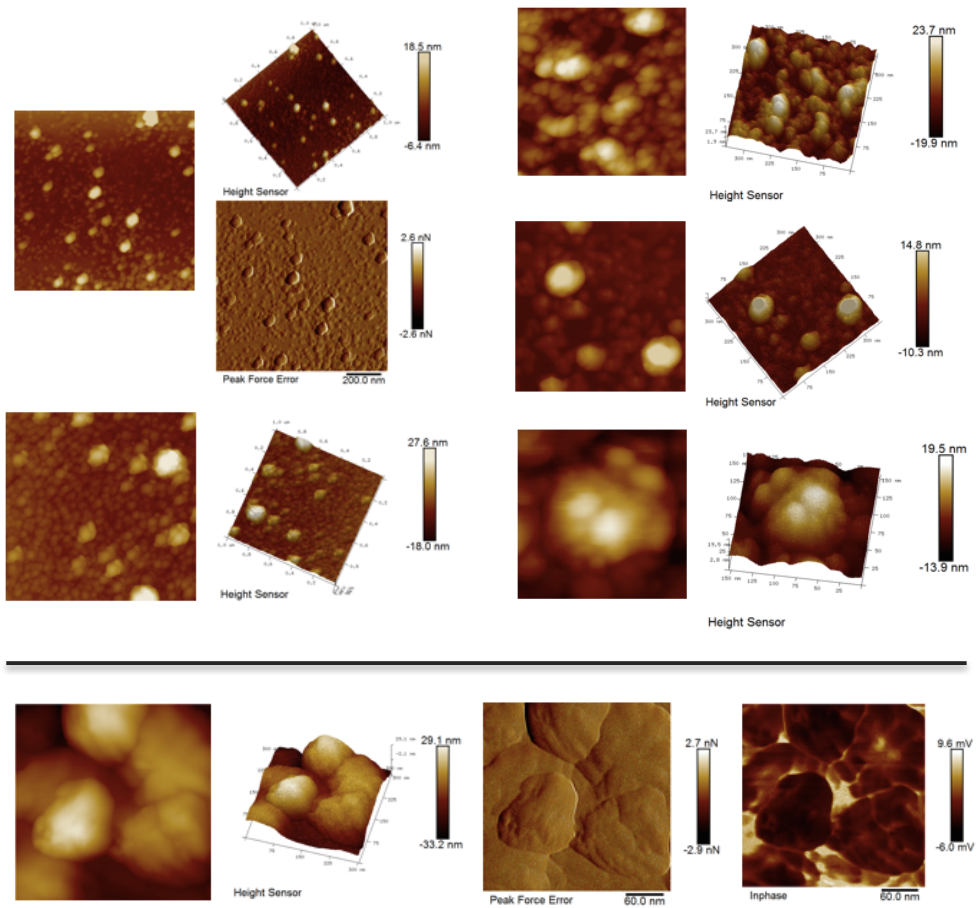


Figure 60. The dispersed FeO_x & SiO_2 NPs as measured by AFM.

4.3 Powder X-Ray Diffraction (PXRD)

In figure 11 the X-ray diffraction spectrum of the sample is shown. With the use of the EVA program, it was matched to SiO_2 and Fe_3O_4 . As mentioned before, earlier research on the subject has determined that some magnetite will be oxidized to maghemite. Some of the peaks that are explained by neither Fe_3O_4 , nor SiO_2 are most likely originating from this fraction $\gamma\text{-Fe}_2\text{O}_3$ present. Since the spectrum mostly matches magnetite, this is probably the most abundant iron oxide present in the NPs.

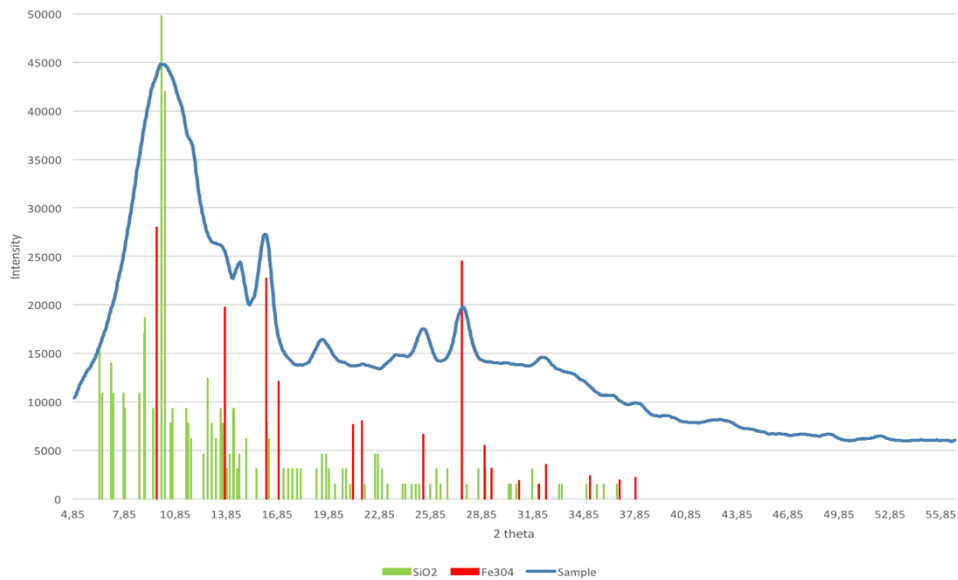


Figure 11. The $\text{FeO}_x/\text{SiO}_2$ NP spectrum as measured by PXRD. The blue line is the sample, the red peaks correspond to Fe_3O_4 and the green peaks correspond to SiO_2 .

4.4 Fourier-Transform Infrared Spectroscopy (FTIR)

Figure 12 shows the FTIR spectrum of the nanoparticles, which confirms the presence of silica and iron oxide.

The absorption band at 575 cm^{-1} is the characteristic Fe-O stretching. There is another Fe-O stretching vibration at 473 cm^{-1} , which overlaps with the bending vibration of Si-O-Si. The other bands that indicate the presence of silica appear at 805 cm^{-1} , $1090\text{-}1100\text{ cm}^{-1}$ and 961 cm^{-1} : the symmetric and asymmetric stretching of Si-O-Si and Si-OH stretching respectively. The two bands at 1645 cm^{-1} and $3450\text{ - }3645\text{ cm}^{-1}$ are attributed to the bending and stretching vibrations of the O-H bond, due to chemically absorbed water and surface hydroxyl groups.

Table 3. Identification of the peaks in the infrared spectrum

Wavenumber (cm^{-1})	Peak identification
473	$\delta(\text{Si-O-Si})$ and $\nu_{\text{as}}(\text{Fe-O})$
575 - 637	$\nu_{\text{s}}(\text{Fe-O})$
805	$\nu_{\text{s}}(\text{Si-O-Si})$
961	$\nu_{\text{s}}(\text{Si-OH})$
1090 - 1100	$\nu_{\text{as}}(\text{Si-O-Si})$
1645	$\delta(\text{O-H})$
3450 - 3645	$\nu_{\text{s}}(\text{O-H})$

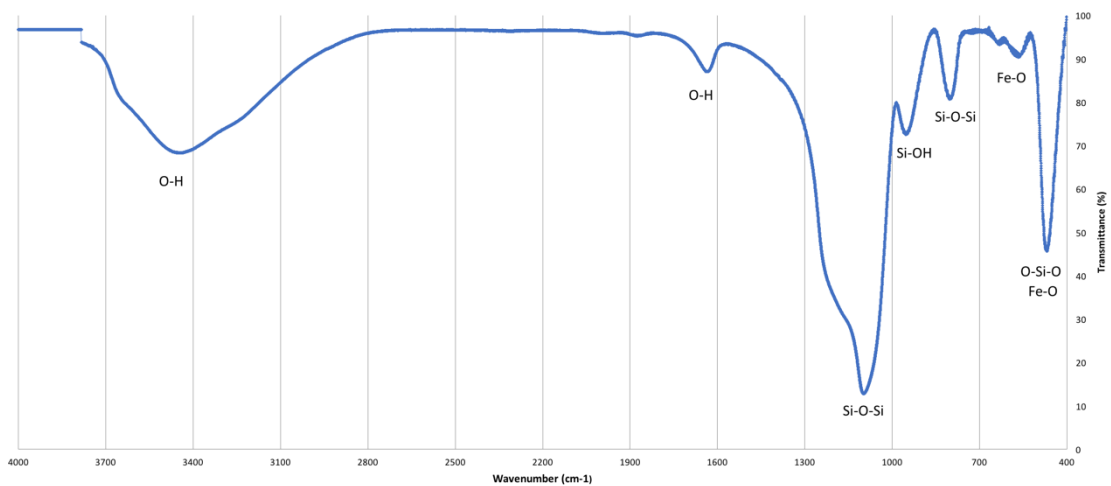


Figure 12. The $\text{FeO}_x\&\text{SiO}_2$ spectrum as measured by FTIR.

4.5 Dynamic Light Scattering (DLS)

In order to be able to analyze the NPs in dispersion, an optimal method needed to be found to get the NPs in a stable solution. Based on a different dispersion method of NM104 particles (ca. 70 nm TiO₂ NPs), the particles were suspended, sonicated at maximum intensity with 15 second intervals and centrifuged at 4400 rpm for 90 minutes. The top half of the tube was pipetted into a new tube and analyzed with DLS. The pH and sonication time were varied to get an optimum, however the dispersion will never be completely stable, as the particles possess magnetic properties and will attract each other.

The tested combinations and results are listed in the table below. Another sample dispersed in NaOH with 10 min sonication time was dispersed after centrifugation, so the average size was not accurate and the result was excluded from the table. The last method was deemed to be ideal, as the NPs were synthesized to be 80 nm. When repeating this method a second time, the average size was found to be 94 nm.

Table 4. *The tested combinations for the optimal dispersion of the FeO_x&SiO₂ NPs.*

Amount weighed (mg)	Sonication time (min)	Water or NaOH (1mM)	pH	Z-average diameter (nm)
50	5	Water (50 mL)	7.06	150
30	10	Water (30 mL)	6.69	163
40	15	Water (40 mL)	6.89	128
40	25	Water (40 mL)	6.92	140
40	5	NaOH (40 mL)	10.29	243
40	15	NaOH (40 mL)	10.10	79

Sonication past 15 minutes gave no further improvement for water. The lowest average size was obtained when dispersing the particles in an alkaline solution.

Some sample were measured after 15 hours to test their stability. As shown in the graph (figure 13), no sample stayed completely stable due to the magnetic particles attracting each other.

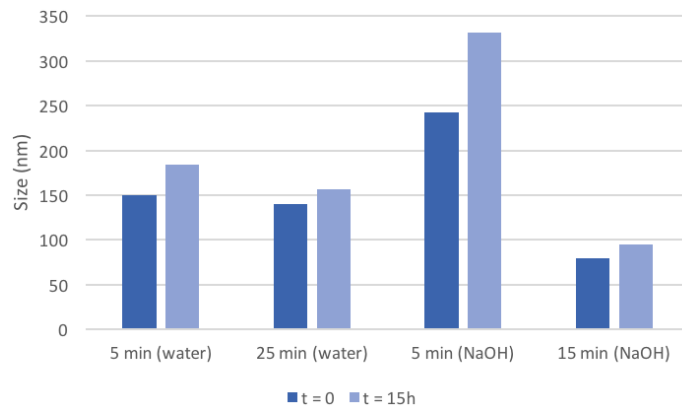


Figure 13. Z-average diameter measured with DLS after 0 and 15 hours of preparation

The size distribution of the dispersed NPs with the optimal method (1 mM NaOH, 15 minutes sonication time) are shown in figure 14, which shows that even though the average size is reported as 79 nm, the sample is very polydisperse.

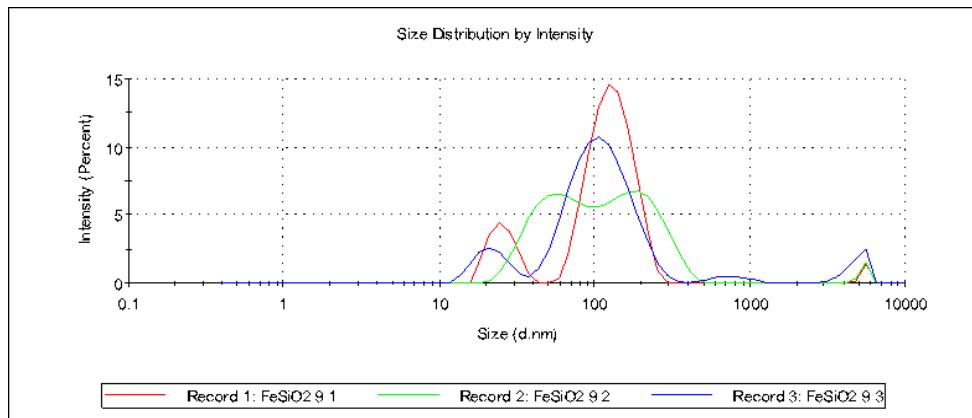


Figure 14. The particle size distribution of the FeOx&SiO₂ NPs as measured with DLS.

4.6 Nanoparticle Tracking Analysis (NTA)

NTA was used on a more newly prepared sample (figure 15) of dispersed NPs and a 10 days old sample (figure 16). More so than in DLS, it shows that the sample is very polydisperse. Even the newer sample, which was less than a day old, aggregation has already started.

Silica is a poor light scatterer (Tuoriniemi et al., 2014) and the concentration was too low to get an accurate reading. This led to poor statistics and a great variation in mean size and total particle concentration. In general, the older sample had a larger mean diameter and larger total concentration. This is because NTA has a reported size detection limit of 30 nm and it has been found that the presence of few large particles reduces the number of small particles detected (Filipe et al., 2010). As a result, the smaller particles in the dispersion aren't counted in the newer sample, while they are aggregated and thus counted in the older sample.

The concentration in particles mL^{-1} was recalculated to $\mu\text{g mL}^{-1}$ to compare with the ICP-MS concentration and the results are shown in table 6. below.

Table 5. Measured size and concentration of the newer and older sample of FeO_x & SiO_2 NPs with NTA.

	Mean size (nm)	Concentration (particles mL^{-1})	Concentration ($\mu\text{g L}^{-1}$)
Newer sample	170	0.10×10^8	138.0
	199	0.14×10^8	298.7
	305	0.16×10^8	1228.9
	305	0.19×10^8	1459.3
Average	245	0.15×10^8	780.0
Older sample	315	0.31×10^8	2622.9
	299	0.26×10^8	1881.4
	385	0.24×10^8	3707.5
	299	0.39×10^8	2882.1
Average	325	0.30×10^8	2758.5

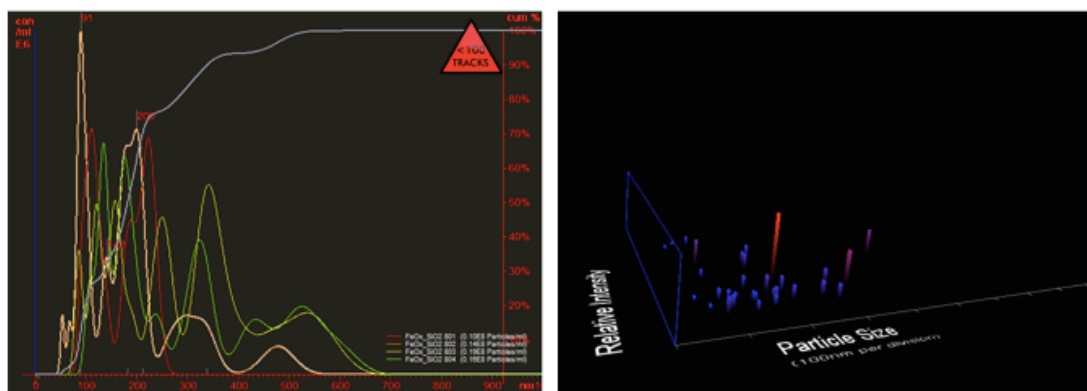


Figure 15. The particle size / concentration plot and particle size / relative intensity 3D plot of the newer sample of $\text{FeO}_x\&\text{SiO}_2$ NPs as measured with NTA (mean size 199 nm and total concentration $0.14 \cdot 10^8$ particles mL^{-1}).

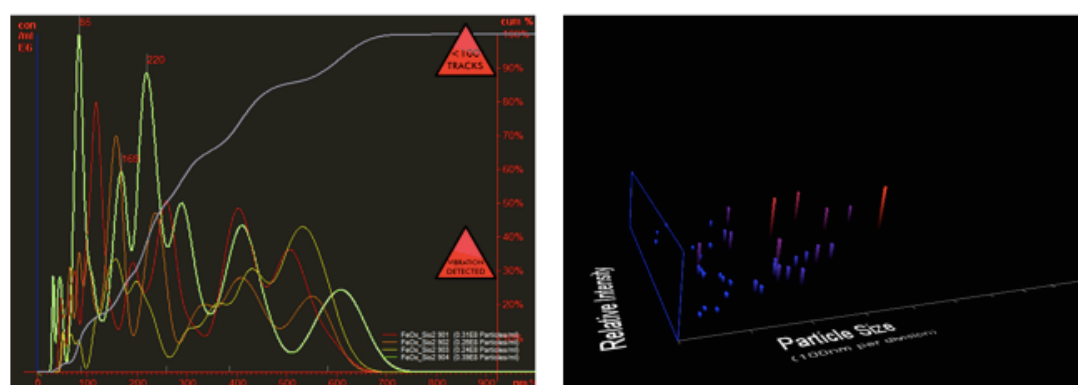


Figure 16. The particle size / concentration plot and particle size / relative intensity 3D plot of the older sample of $\text{FeO}_x\&\text{SiO}_2$ NPs as measured with NTA (mean size 299 nm and total concentration $0.39 \cdot 10^8$ particles mL^{-1}).

4.7 Inductively Coupled Plasma Mass Spectrometry (ICP-MS)

Due to problems with the ICP-MS instrument, it was not possible to measure the iron oxide NPs with spICP-MS. At the most optimal settings, quite high backgrounds and poor sensitivities were still obtained with NH₃ gas in the reaction mode, making it impossible to measure in single particle mode, which only operates in pulse counting mode and thus can't handle these high intensities. He-gas in the collision mode with KED gave better results, but isn't available yet for spICP-MS. This means it was only possible to measure the total iron concentration with ICP-MS. The sample was diluted 100x, 10x and 2x to get a good concentration and the results are shown in table 7.

Table 6. *Measured total concentration of FeO_x&SiO₂ NPs with ICP-MS.*

Dilution factor	Total concentration (µg L ⁻¹)
100x	2936,8
10x	2980,7
2x	2617,9
<i>Average:</i> 2845,1	

The ICP-MS results complement the NTA results of the older NTA sample the most, which further indicates NTA missed a lot of small particles in the newer sample.

5 Conclusion

A summary of the approximate sizes obtained with the different methods can be found in table 8. Since the particles were found to be more polydisperse than expected and the dispersion aggregates quickly, no 'correct' size can be determined.

Table 7. Comparison of the measured mean sizes obtained with ESEM-EDS, AFM, DLS and NTA of the FeO_x & SiO_2 NPs.

Size objective during synthesis: 80 nm		
HR-TEM result: 100 nm		
Method	Size non-dispersed NPs (nm)	Size dispersed NPs (nm)
ESEM-EDS	~ 738	~ 627
AFM	~ > 90	~ > 30
DLS	/	87
NTA	/	245

While reports have concluded that ESEM-EDS gives reliable sizes (Tuoriniemi et al., 2014), the resolution of the particular instrument used for this thesis was too low for accurate size measurements. AFM resulted in smaller particles, but gave a good result for the non-dispersed NPs, considering a non-aggregated NP could be found. The dispersed NPs in AFM shifted too easily to be measured. Due to the low concentration and size detection limit of 30 nm, NTA did not give accurate results, while the average diameter with DLS, which has a size detection limit of only 1 nm, came closer to the expected value. For bigger particles NTA is still the better option, especially for polydisperse samples.

The iron oxide core-shell NPs, coated with a silica layer were analysed and characterized with ESEM-EDS, AFM, PXRD, FTIR, NTA, DLS and ICP-MS. It can be concluded that the iron oxide nanoparticles are successfully encapsulated by a silica

layer. While the core mostly consists of magnetite (Fe_3O_4), some oxidation to maghemite ($\gamma\text{-Fe}_2\text{O}_3$) has taken place. An external investigation for separation based on magnetic properties to determine the exact fraction that has been oxidized and a method development with spICP-MS is recommended for supplementary research. These nanoparticles have already been proven successful in a wide range of applications, such as magnetic targeting drug delivery, enzyme immobilization, water purification, hydrometallurgy of REE's, catalysis, *etc.* Further development of these promising applications should definitely be done.

References

- BRITANNICA, E. 2017. Brownian motion. Encyclopædia Britannica, inc.
- CORNELL, R. M. & SCHWERTMANN, U. 2003. *The Iron Oxides: Structure, Properties, Reactions, Occurrences and Uses*, Wiley.
- COURSE-MATERIAL 2015. Practical Guide in PXRD and ESEM studies (materials for the soil and water chemistry course). Swedish University of Agricultural Sciences.
- DENG, Y., QI, D., DENG, C., ZHANG, X. & ZHAO, D. 2008. Superparamagnetic High-Magnetization Microspheres with an Fe₃O₄@SiO₂ Core and Perpendicularly Aligned Mesoporous SiO₂ Shell for Removal of Microcystins. *Journal of the American Chemical Society*, 130, 28-29.
- DOMINGOS, R. F., BAALOUSHA, M. A., JU-NAM, Y., REID, M. M., TUFENKJI, N., LEAD, J. R., LEPPARD, G. G. & WILKINSON, K. J. 2009. Characterizing Manufactured Nanoparticles in the Environment: Multimethod Determination of Particle Sizes. *Environmental Science & Technology*, 43, 7277-7284.
- ENCYCLOPEDIA 2018a. Energy Dispersive Spectroscopy. *World of Forensic Science*. Encyclopedia.com.
- ENCYCLOPEDIA 2018b. Silicon Dioxide. *Chemical Compounds*. Encyclopedia.com.
- ESMAEILPOUR, M., SARDARIAN, A. R. & JAVIDI, J. 2012. Schiff base complex of metal ions supported on superparamagnetic Fe₃O₄@SiO₂ nanoparticles: An efficient, selective and recyclable catalyst for synthesis of 1,1-diacetates from aldehydes under solvent-free conditions. *Applied Catalysis a-General*, 445, 359-367.
- FILIPPE, V., HAWE, A. & JISKOOT, W. 2010. Critical Evaluation of Nanoparticle Tracking Analysis (NTA) by NanoSight for the Measurement of Nanoparticles and Protein Aggregates. *Pharmaceutical Research*, 27, 796-810.
- HANEDA, K. & MORRISH, A., H. 1977. Magnetite to maghemite transformation in ultrafine particles. *J. Phys. Colloques*, 38, C1-321-C1-323.
- HOLBROOK, R. D., GALYEAN, A. A., GORHAM, J. M., HERZING, A. & PETTIBONE, J. 2015. Chapter 2 - Overview of Nanomaterial Characterization and Metrology. In: BAALOUSHA, M. & LEAD, J. R. (eds.) *Frontiers of Nanoscience*. Elsevier.
- HUI, C., SHEN, C. M., TIAN, J. F., BAO, L. H., DING, H., LI, C., TIAN, Y. A., SHI, X. Z. & GAO, H. J. 2011. Core-shell Fe₃O₄@SiO₂ nanoparticles synthesized with well-dispersed hydrophilic Fe₃O₄ seeds. *Nanoscale*, 3, 701-705.
- LARSSON, M., HILL, A. & DUFFY, J. 2012. Suspension stability; why particle size, zeta potential and rheology are important. *Ann. Trans. Nordic Rheol. Soc.*, 20, 209-214.
- LEGARIA, E. P. 2018. *Nanotechnology for hydrometallurgy*. Doctoral Thesis, Swedish University of Agricultural Sciences.
- LEGARIA, E. P., TOPEL, S. D., KESSLER, V. G. & SEISENBAEVA, G. A. 2015. Molecular insights into the selective action of a magnetically removable complexone-grafted adsorbent. *Dalton Transactions*, 44, 1273-1282.
- MAY, T. W. & WIEDMEYER, R. H. 1998. A table of polyatomic interferences in ICP-MS. *Atomic Spectroscopy*, 19, 150-155.

- MONTANO, M. D., MAJESTIC, B. J., JAMTING, A. K., WESTERHOFF, P. & RANVILLE, J. F. 2016. Methods for the Detection and Characterization of Silica Colloids by Microsecond spICP-MS. *Analytical Chemistry*, 88, 4733-4741.
- MURUGADOSS, S., LISON, D., GODDERIS, L., VAN DEN BRULE, S., MAST, J., BRASSINNE, F., SEBAIHI, N. & HOET, P. H. 2017. Toxicology of silica nanoparticles: an update. *Archives of Toxicology*, 91, 2967-3010.
- PAVIA, D. L., LAMPMAN, G. M., KRIZ, G. S. & VYVYAN, J. A. 2008. *Introduction to Spectroscopy*, Cengage Learning.
- POGORILYI, R., MELNYK, I., ZUB, Y., CARLSON, S., DANIEL, G., SVEDLINDH, P., SEISENBAEVA, G. & KESSLER, V. 2014. New product from old reaction: uniform magnetite nanoparticles from iron-mediated synthesis of alkali iodides and their protection from leaching in acidic media. *Rsc Advances*, 4, 22606-22612.
- STOBER, W., FINK, A. & BOHN, E. 1968. Controlled growth of monodisperse silica spheres in micron size range. *Journal of Colloid and Interface Science*, 26, 62-&.
- SUN, S. & ZENG, H. 2002. Size-Controlled Synthesis of Magnetite Nanoparticles. *Journal of the American Chemical Society*, 124, 8204-8205.
- TANNER, S. D., BARANOV, V. I. & BANDURA, D. R. 2002. Reaction cells and collision cells for ICP-MS: a tutorial review. *Spectrochimica Acta Part B-Atomic Spectroscopy*, 57, 1361-1452.
- THOMAS, R. 2002. A beginner's guide to ICP-MS - Part IX - Mass analyzers: Collision/reaction cell technology. *Spectroscopy*, 17, 42-+.
- TOPEL, S. D., LEGARIA, E. P., TISEANU, C., ROCHA, J., NEDELEC, J.-M., KESSLER, V. G. & SEISENBAEVA, G. A. 2014. Hybrid silica nanoparticles for sequestration and luminescence detection of trivalent rare-earth ions (Dy³⁺ and Nd³⁺) in solution. *Journal of Nanoparticle Research*, 16, 2783.
- TUORINIEMI, J., JOHNSON, A., HOLMBERG, J. P., GUSTAFSSON, S., GALLEGU-URREA, J. A., OLSSON, E., PETTERSSON, J. B. C. & HASSELLOV, M. 2014. Intermethod comparison of the particle size distributions of colloidal silica nanoparticles. *Science and Technology of Advanced Materials*, 15, 10.
- WANG, L. A., NEOH, K. G., KANG, E. T. & SHUTER, B. 2011. Multifunctional polyglycerol-grafted Fe₃O₄@SiO₂ nanoparticles for targeting ovarian cancer cells. *Biomaterials*, 32, 2166-2173.
- WILKINSON, K. J. & LEAD, J. R. 2007. *Environmental Colloids and Particles: Behaviour, Separation and Characterisation*, England, John Wiley & Sons Ltd.

Acknowledgements

Special thanks go out to Gulaim Seisenbaeva for helping with all the different methods and always answering my questions and to Ievgen Pylypchuk for assisting with NTA.

Also a big thank you to Jani Tuoriniemi and Geert Cornelis for helping with ICP-MS and assisting me where needed.